3D-Engineered Scaffolds to Study Microtubes and Localization of Epidermal Growth Factor Receptor in Patient-Derived Glioma Cells

Barin, Nastaran; Balcioglu, Hayri E.; de Heer, Iris; de Wit, Maurice; Lamfers, Martine L.M.; van Royen, Martin E.; French, Pim J.; Accardo, Angelo

Important note
To cite this publication, please use the final published version (if applicable).
Please check the document version above.

3D-Engineered Scaffolds to Study Microtubes and Localization of Epidermal Growth Factor Receptor in Patient-Derived Glioma Cells

Nastaran Barin, Hayri E. Balcioglu, Iris de Heer, Maurice de Wit, Martine L. M. Lamfers, Martin E. van Royen, Pim J. French,* and Angelo Accardo*

A major obstacle in glioma research is the lack of in vitro models that can retain cellular features of glioma cells in vivo. To overcome this limitation, a 3D-engineered scaffold, fabricated by two-photon polymerization, is developed as a cell culture model system to study patient-derived glioma cells. Scanning electron microscopy, (live cell) confocal microscopy, and immunohistochemistry are employed to assess the 3D model with respect to scaffold colonization, cellular morphology, and epidermal growth factor receptor localization. Both glioma patient-derived cells and established cell lines successfully colonize the scaffolds. Compared to conventional 2D cell cultures, the 3D-engineered scaffolds more closely resemble in vivo glioma cellular features and allow better monitoring of individual cells, cellular protrusions, and intracellular trafficking. Furthermore, less random cell motility and increased stability of cellular networks is observed for cells cultured on the scaffolds. The 3D-engineered glioma scaffolds therefore represent a promising tool for studying brain cancer mechanobiology as well as for drug screening studies.

1. Introduction

Gliomas are the most common primary malignant tumors of the central nervous system with poor patient survival rates.[1] One contributor to the absence of novel effective therapies is the lack of cell culture models that can faithfully capture the native glioma phenotype[2,3] even despite increasing use of patient-derived cell cultures (that more accurately capture the cancer

cell genotypes compared to standard cell lines).[4,5] Current in vitro models for example, rapidly lose high copy epidermal growth factor receptor (EGFR) amplification and have limited ability to monitor cells and (microtube-based) networks.[6,7] High copy EGFR amplification and microtube-based networks are two important features that are known to promote glioma progression.[8–11] To further study the role of microtubes in glioma progression and also the potential of EGFR-targeting treatments in glioma, in-vitro cell culture models that can retain these features are needed.[10] Currently, in vitro cell culture research predominantly involves the use of 2D planar surfaces. Although these 2D surfaces are cheap, easy-to-use, and reproducible, they often do not mimic the 3D spatial configuration of cells in real tissues. Indeed, cells behave differently in 3D environments[12,13] and can have differences in terms of cellular morphology, formation of cell–cell junctions, cell proliferation, gene and protein expression levels, and even in responses to treatments.[14–17] 3D tumor spheroids, which are generally employed for glioma research, can overcome these limitations by better mimicking tissue-like features. However, they are difficult to monitor especially when analyzing subcellular structures like microtubes.[6,14,16]

N. Barin, A. Accardo
Department of Precision and Microsystems Engineering
Delft University of Technology
Mekelweg 2, Delft 2628 CD, The Netherlands
E-mail: a.accardo@tudelft.nl

N. Barin, I. de Heer, M. de Wit, P. J. French
Department of Neurology
Erasmus MC Cancer Institute
University Medical Center
Doctor Molewaterplein 40, Rotterdam 3015 GD, The Netherlands
E-mail: p.french@erasmusmc.nl

H. E. Balcioglu
Department of Medical Oncology
Erasmus MC Cancer Institute
University Medical Center
Doctor Molewaterplein 40, Rotterdam 3015 GD, The Netherlands

M. L. M. Lamfers
Department of Neurosurgery
Erasmus MC Cancer Institute
University Medical Center
Doctor Molewaterplein 40, Rotterdam 3015 GD, The Netherlands

M. E. van Royen
Department of Pathology
Erasmus MC Cancer Institute
University Medical Center
Doctor Molewaterplein 40, Rotterdam 3015 GD, The Netherlands

ADVANCED
SCIENCE NEWS
www.advancedsciencenews.com

NANO · MICRO
small
www.small-journal.com

With technological advances, 3D cell culturing (growing cells in three dimensions) on structures created by micro- and nanofabrication has become an appealing alternative.[18–20] The most accurate additive manufacturing processes for the creation of cell scaffolds are two-photon polymerization (2PP) and stereolithography.[18,21,22] 2PP is a relatively recent light-assisted direct-writing fabrication technique based on the nonlinear two-photon absorption of near-infrared photons from a femtosecond pulsed laser source. Using this technique, infrared femtosecond laser pulses are focused onto an organic prepolymer material that is absorptive in the UV radiation range but nonabsorptive in the infrared one.[20,23] This mechanism is tuned to photopolymerize the exposed material in extremely confined volumes called voxels.[23] The advantages of the 2PP technique include: high resolution (up to 100 nm), high reproducibility, precise control of intricate structural features, and freedom in architecture design.[20,24,25] Importantly, the recent development of a biocompatible and low-autofluorescent methacrylate photosensitive polymer (IP-Visio) for 2PP has facilitated the use of this approach for life science applications.[23,26,27]

Here, we have studied patient-derived glioma cells cultured on biomimetic 3D-engineered IP-Visio microscaffolds, fabricated by the 2PP technique, and compared them to standard 2D control models. Our results show that a standard glioma cell line (U-87) as well as four patient-derived glioma cultures can efficiently adhere and colonize the structures. Compared to 2D models, our 3D-engineered glioma microenvironment more closely resembled in vivo glioma cellular features including nucleus size, and protrusion width. A major advantage of our model system is that it enables more accurate detection of individual cells, their protrusions, and intracellular trafficking. Furthermore, real-time microscopy also enabled the assessment of cell mobility and demonstrated reduced speed of cells and increased stability of cellular networks in 3D versus 2D. The developed 3D-engineered scaffold therefore provides a new suitable model to study glioma cells with advantages over the traditional 2D models.

2. Results and Discussion

2.1. Design and Fabrication of the 3D-Engineered Scaffolds Inspired by Microvessel Geometries

The design of the 3D scaffolds (**Figure 1**a) was inspired by the features of blood vessels present in the in vivo glioma environment as it is known how glioma cells migrate, proliferate, and cluster especially at the vascular branch points.[6,28] A porous design was selected to allow cell migration within the structures and to facilitate the diffusion of nutrients. The pore size was chosen to be larger than the cell nuclei to allow for cell invasion but small enough to allow for cellular network formation.[29] To avoid shadowing which would hamper imaging of the bottom and middle layers of the scaffolds during confocal microscopy, highly dense structures were not considered.

The base element of the scaffolds consisted of rods connected as cubic unit cells with one additional interconnecting diagonal rod (Figure 1b). Cylindrical rods were chosen as the building blocks of the unit cells to resemble the circular

cross-section of the blood vessels. Diagonal rods were added to provide angles in the structure that resemble those observed in blood vessels.[6,28] Each scaffold consisted of multiple unit cells arranged to form a pyramid. The scaffolds featured a rod size of 10 μm and a pore size of 50 μm × 50 μm. The overall dimension of each scaffold was 370 μm × 370 μm × 190 μm. For some experiments, an alternative scaffold was used with the same unit cells but with an inverted unit cell arrangement that resulted in the presence of a cavity inside the scaffold to study the span of cellular protrusions (Figure S1a,b, Supporting Information). The scaffolds were fabricated by 2PP following the routine procedure of the 2PP fabrication methodology, which is described step by step in the Experimental Section. To obtain accurate scaffold geometries and overcome technical issues, we optimized several manufacturing process steps, which are described hereafter.

DeScribe software (Nanoscribe proprietary software to define printing parameters such as laser power, writing speed, hatching/slicing and to simulate the 2PP fabrication steps) considers surfaces with gaps or sharp edges as defective and attempts to repair them,[30] which led to undesirable filled pores (Figure S2a, Supporting Information). We found that pore filling could be prevented via rounding the corners in our design. In addition, as the voxel size is larger along the Z direction than the X and Y directions (where Z is the direction of the laser beam), pores along the Z-axis were clogged in the fabricated scaffolds (Figure S2b, Supporting Information). To prevent this, we changed the cross-section of the top rods of the unit cells from circular to oval, making the circular structures narrower along the Z direction (Figure S2c, Supporting Information). An additional complication was the occasional delamination of the scaffolds after exposure to cell culture media (Figure S3a, Supporting Information). To address this issue and to increase the stability of the 3D structures (Figure S3b, Supporting Information), the cross-sections of the rods connected to the substrate were changed to a flattened bottom (semicircle on a pedestal, Figure S3c, Supporting Information). For 2D structures, pedestals of 500 μm × 500 μm × 10 μm were chosen. Four pedestals were connected to each other by their corners (Figure S1c, Supporting Information) to prevent delamination.

The most important printing parameters that needed tuning were the scan speed, laser power, hatching, and slicing. Hatching is the spacing distance between voxels in the X–Y plane, while slicing is the spacing distance between voxels along the Z direction.[31] Decreasing slicing and hatching values increased the shape accuracy and steadiness of the structures but noticeably increased the printing time. For the final 3D scaffolds, 10 000 μm s^{-1} scan speed and 60% laser power (100% laser power is 50 mW) were chosen to provide a suitable combination of precision and stability. A 50 000 μm s^{-1} scan speed and 80% laser power provided a suitable 2D pedestal quality. The slicing and hatching values for the scaffolds were both 0.5 μm. The corresponding values for the pedestals were 1 and 0.5 μm, respectively.

Both 3D scaffolds and 2D pedestals exceeded the addressable printing range of the galvanometric mirrors of the 2PP-printer setup (the galvanometric mirrors scan the laser beam laterally while vertical movements are carried out with piezoactuators). Therefore, the structures needed to be split into smaller unit
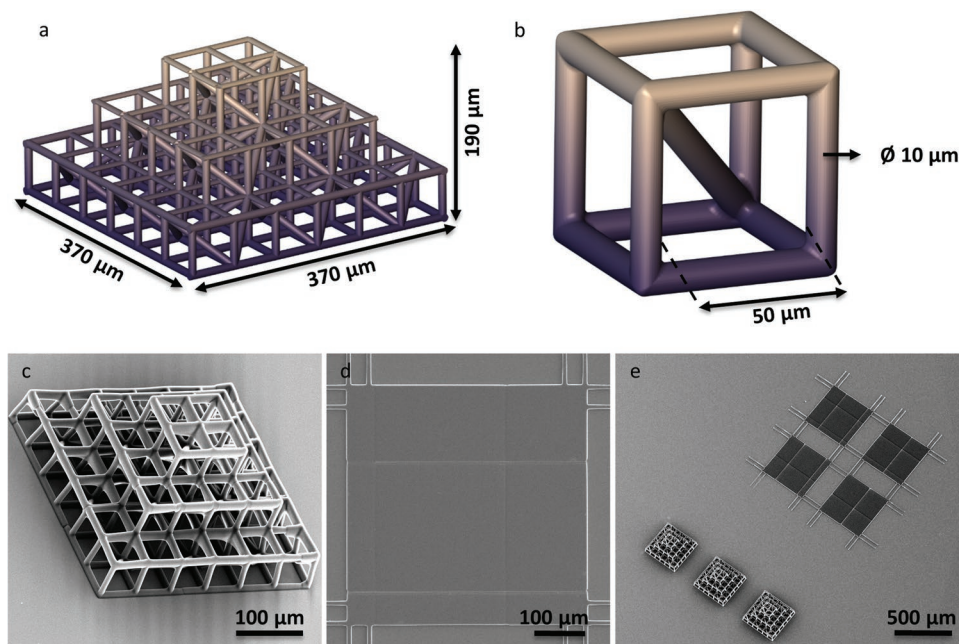
Figure 1. Design of the 3D and 2D microenvironments. a) Design of the 3D-engineered scaffolds. b) Scaffold unit. c) SEM micrograph of the fabricated 3D-engineered scaffold. d) SEM micrograph of the fabricated 2D pedestal. e) Three scaffolds and four pedestals constituting one "sample set".

blocks (block splitting) and these blocks needed to be bonded together during the printing process (stitching). Block splitting was avoided at locations where it led to the creation of overhanging rods (Movies S1 and S2, Supporting Information). In order to increase the adhesion between blocks, an angled interface between blocks was selected instead of an orthogonal interface (Figure S4, Supporting Information). The acceptable angle value was found by printing scaffolds and pedestals with varying angles. The suitable stitching angles for 2D pedestals and 3D scaffolds were found to be 45° and 15°, respectively. The stitched blocks featured some overlap in order to avoid disjoined blocks caused by unpolymerized resin. The suitable overlap between stitched blocks in the X, Y, and Z directions were found to be 3, 3, and 2 µm for the 2D pedestals, and 1, 1, and 2 µm for the 3D scaffolds, respectively. Representative scanning electron microscopy (SEM) images of the final structures are shown in Figure 1c,d. Three replicas of the scaffold as well as four replicas of 2D flat pedestals were printed on each substrate creating one sample set (Figure 1e). The fabrication time for each sample set was 95 min. The structures were then coated with a Cultrex extracellular matrix coating (see Experimental Section).

Our approach aims at resembling the geometrical features of the brain microvessels, however one of its limitations is the relatively high stiffness of the scaffolds' material (≈1 GPa) compared to that of the brain (ranging from 0.1 to 1 kPa).[32] Developing materials for 2PP with lower Young's modulus can be further investigated to overcome current challenges. The challenges of fabricating complex geometries with soft materials (such as hydrogels) include higher tendency to collapse, difficulties handling the load of cells, and lower feature resolution.[33] An alternative option worth exploring is using structures in which cells perceive a low effective shear

modulus[34] or encapsulating cells (bioprinting) whithin 2PP-manufactured scaffolds. Overcoming the cytotoxic effects of photo initiators has been one of the major challenges of 2PP bioprinting. Although reports of such cultures have been published, these materials are not yet commercially available.[35,36] In addition to mechanical cues, cells respond also to topographical cues,[13,37] therefore, the effects of different geometrical features (e.g. pore size, surface nanotopography, rod size, curvature) on the behavior and morphology of glioma cell can be investigated.[38]

2.2. Colonization of the 3D Scaffolds by Patient-Derived Glioma Cells

To test the suitability of the fabricated structures for glioma cell culture experiments, we first cultured a standard cell line (U-87) on the 3D scaffolds and the 2D pedestals. As these cultures readily colonized the scaffolds (Figure S5, Supporting Information), we subsequently cultured four patient-derived glioma cell cultures (GS-580, GS-827, GS-830, and GS-921) on the structures. All four patient-derived cultures were able to successfully colonize the scaffolds and the 2D pedestals as shown by confocal imaging (**Figure 2**a–c; Movie S3, Supporting Information). SEM micrographs showed that cells formed long protrusions and clearly invaded the inner regions of the scaffolds (Figure 2d–f). These protrusions were frequently present between the building blocks of the scaffolds (Figure 2e). Interestingly, some of these interconnecting protrusions were suspended within the 3D structure (Figure 2e,f). Such suspended protrusions were not observed in the alternative 3D design (Figure S1a, Supporting Information) with gaps exceeding 100 µm (Figure S6, Supporting Information).
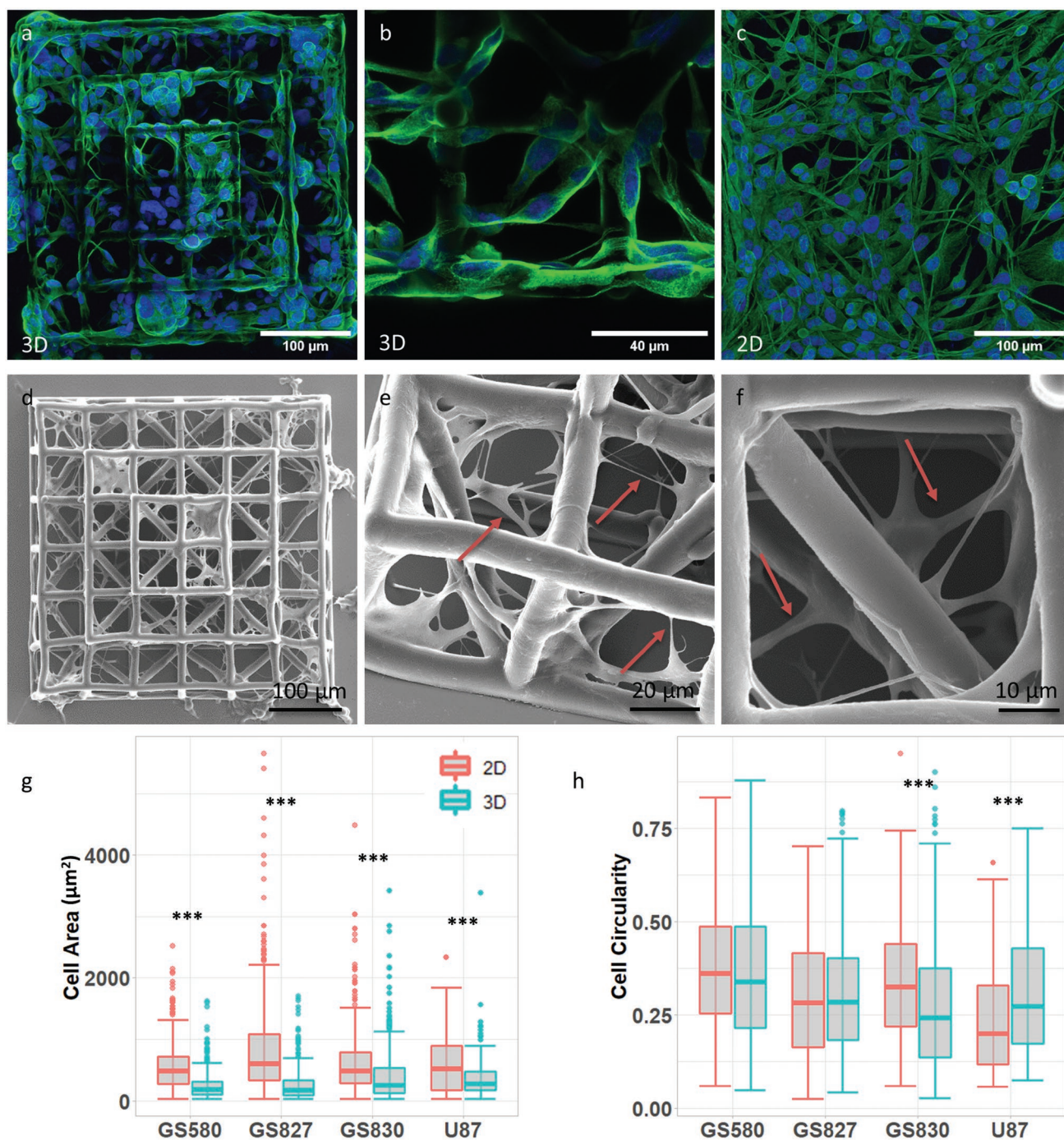
Figure 2. Characterization of patient-derived glioma cells cultured on 2D pedestals and 3D scaffolds. Confocal images of GS-830 patient-derived glioma cells on a,b) 3D scaffolds and c) 2D pedestals (Blue: nuclei; Green: tubulin). d) SEM image of GS-830 cells cultured on the 3D scaffolds. e,f) Zoomed in SEM image of the GS-830 cells on the 3D scaffolds showing that the cells have reached the inner units. Red arrows denote examples of glioma cell protrusions. g,h) Boxplots comparing morphological differences between cells cultured in 2D and 3D. g) Cell area and h) cell circularity. Boxplots display the median, interquartile range (IQR) with the whiskers drawn at 1.5IQR. Statistical significance is indicated by $p < 0.001(***)$. Sample size (n) for GS580, GS287, GS830, and U87 are 683, 937, 890, and 294 respectively. Two independent experimental replicates (one replicate for U-87 experiments) were included.

2.3. Cytoskeletal and Nuclear Morphological Differences between Glioma Cells Cultured on 3D Scaffolds and 2D Pedestals

To determine whether the scaffolds provided a suitable model system for glioma research, we then compared morphological features of GS-830, GS-827, GS-580, and U-87 cells cultured on 3D versus 2D structures. Cellular morphology was studied in two independent experimental replicates (one replicate for U-87 experiments) using confocal fluorescent images of the cells stained for nuclei and tubulin.
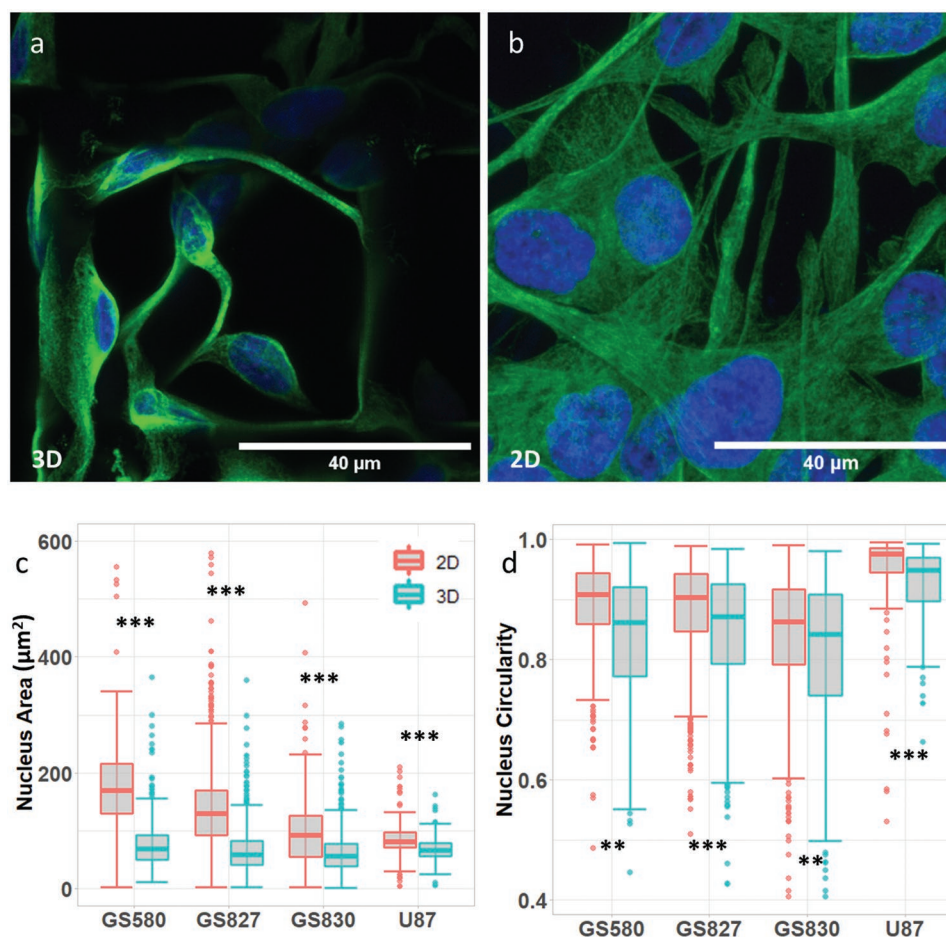
Figure 3. Characterization of patient-derived glioma cell nuclei cultured on 2D pedestals and 3D scaffolds. Confocal images of GS-830 patient-derived glioma cells cultured on a) 3D scaffolds and b) 2D pedestals (Blue: nuclei; Green: tubulin). c,d) Boxplots comparing morphology differences between cells cultured in 2D and 3D structures. c) Nuclear area and d) nuclear circularity. Boxplots display the median, IQR with the whiskers drawn at 1.5IQR. Statistical significance is indicated by $p < 0.01$ (**) and $p < 0.001$(***). Sample size (n) for GS580, GS287, GS830, and U87 are 970, 2059, 1395, and 286, respectively. Two independent experimental replicates (one replicate for U-87 experiments) were included.

Interestingly, we found that cells grown on 2D pedestals had larger areas compared to those on the 3D scaffolds (Figure 2g). We did not observe consistent differences between 2D pedestals and 3D substrates in terms of cellular circularity (Figure 2h). In addition to cellular morphology, we also studied nuclear morphology. For all cell cultures, nucleus area of cells cultured on 2D pedestals were larger compared to those on the 3D scaffolds and were on average more circular (**Figure 3**a–d). Although the larger cell and nuclear areas on 2D pedestals most likely pointed to the flatter morphology of cells on 2D surfaces, such morphological differences, especially those related to the nuclei, can be important for replicating the behavior of glioma cells in vivo.[39,40]

The nucleus, through cytoskeleton and cell–matrix adhesions, is physically coupled to the extracellular matrix. In this way, forces can be transmitted from the cytoskeleton to the nucleus, and the external mechanical cues on the cell can affect the shape of the nuclear envelope.[41] This can affect the nuclear function by altering: chromatin condensation and organization (thereby directing cells toward differential gene expression), translocation of transcriptional regulators, accessibility of histone

modifying enzymes to the chromatin and their distribution in the nucleoplasm, and nuclous membrane permeability and rupture.[41–47] Furthermore, nuclei morphology is frequently altered in cancer cells and many cancers can even be graded based on the nucleus size.[48] Particularly, for high-grade glioma tumor cells, previous studies reported how nuclear size and shape are significantly related to the survival time of patients.[39,49]

To compare our results to in vivo values, we studied the morphology of nuclei in six glioma tumor samples. Three grade 3 and three grade 4 formalin-fixed paraffin-embedded (FFPE) glioma tumor tissue sections were analyzed for nuclei area and circularity. The measured average nuclear area on tissue sections ($55.72 \pm 27.79\ \mu m^2$) was nearly identical to previously reported (i.e., $55.22 \pm 13.48\ \mu m^2$)[49] and was close to the value observed for tumor cells cultured on 3D scaffolds ($67.51 \pm 38.19\ \mu m^2$, p-value < 0.0001). Nucleus areas on 3D scaffolds and on tissue sections were both smaller than the nucleus area on 2D pedestals ($130.21 \pm 75.72\ \mu m^2$, both p-values < 0.0001). However, nuclei on our 3D scaffolds on average were less circular (0.84 ± 0.11) compared to those on 2D pedestals (0.88 ± 0.09, p-value < 0.0001) and tissue sections
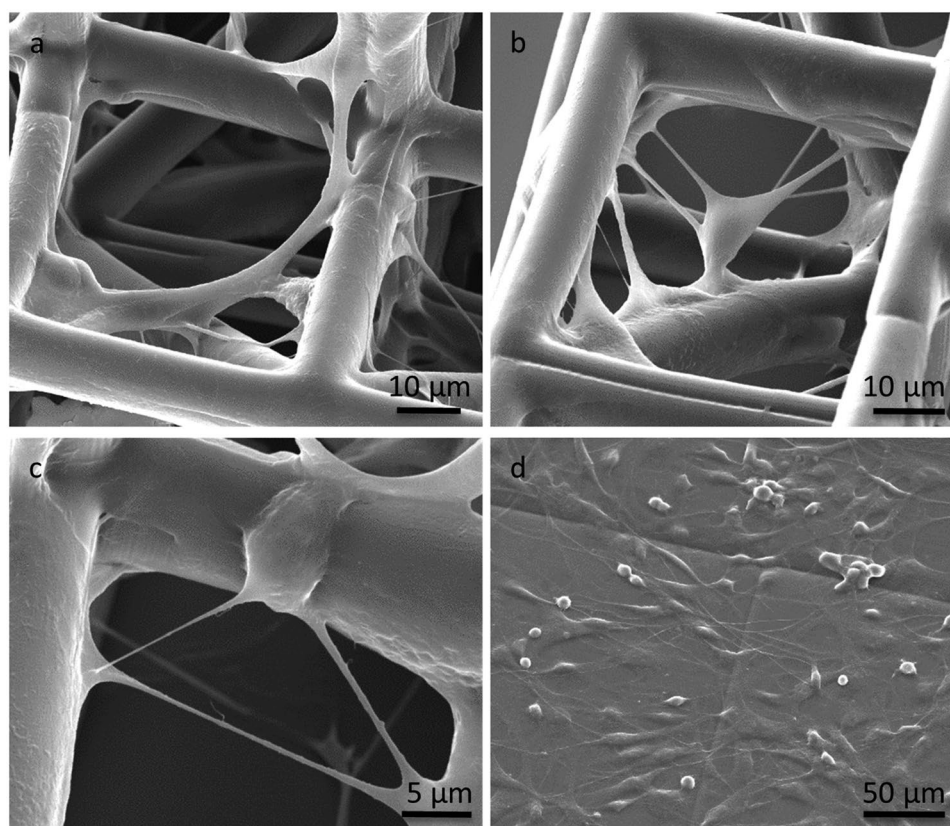
Figure 4. SEM images of patient derived glioma cells cultured on 2D pedestals and 3D scaffolds showing microtube-like protrusions. a) Cells cultured on the 3D scaffold showing several tube-like protrusions with widths in the b) microscale and c) in the nanoscale. d) Cell protrusions on the 2D pedestals are harder to detect.

(0.89 ± 0.07, p-value < 0.0001). Yet, it should be noted that tissue sectioning likely leads to an underestimation of nucleus area and overestimation of nucleus roundness compared to Z projection of stacks of images as used for our scaffold and pedestal analysis. Moreover, the increased cell circularity for tumor cells on tissue may be related to their more compact microenvironment.

2.4. Microtube Morphological Discrepancies between 3D Scaffolds and 2D Pedestals

To further examine the relevance of our culture model, we characterized the presence of microtube like protrusions. Microtubes are long and thin cellular protrusions that allow formation of functional cellular networks.[8] These protrusions enable aggressive tumor invasion and make gliomas more therapy resistant.[6,8] SEM micrographs showed intercellular tube-like protrusions on both 3D scaffolds and 2D pedestals (**Figure 4**a–d). Protrusions longer than 50 µm were observed on the 3D scaffolds (Figure 4a), with multiple protrusions departing from a single cell (Figure 4b). These protrusions were easier to observe on 3D scaffolds due to their suspended nature. In particular, nanotubes, tube-like protrusions at the nanoscale (<1 µm wide), were observed only on 3D scaffolds (Figure 4c) and not on 2D pedestals (Figure 4d).

We then further studied these protrusions with immunostaining (**Figure 5**a–d). Confocal fluorescent images with tubulin and nucleus staining confirmed the presence of tube-like protrusions (Figure 5a,b). These protrusions were observed on both 2D pedestals and 3D scaffolds for all patient-derived cultures and U-87 standard cell line (additional images in Figure S7, Supporting Information). In order to characterize the nature of microtubes, we stained GS-830 cells for GAP-43, which is a protein reported as a molecular driver for microtubes and previously employed to identify these protrusions.[50,51] Cells cultured on 3D scaffolds and 2D pedestals expressed GAP-43 in membranes and protrusions (Figure 5c,d). GAP-43 did not seem to exclusively stain the tube-like protrusions in our experiments.[6,50] Instead, it was detected throughout the cell membranes and was more prominent at the end-cone of protrusions, consistent with its function in neurons.[9,50,52]

We then employed the confocal images to quantify the size of these protrusions (Figure 5e,f). Overall the geometrical characteristics of the observed protrusions matched that of microtubes or nanotubes.[51] In two of the cell cultures, the recorded average length of the microtube-like protrusions was higher in 2D pedestals versus the 3D scaffolds (Figure 5e). All cultures had average protrusion lengths in the range of 38 to 60 µm. GS-827 showed longer protrusion lengths up to 241 µm in 2D pedestals and 179 µm in 3D scaffolds. However, it should

**ADVANCED
SCIENCE NEWS**

www.advancedsciencenews.com
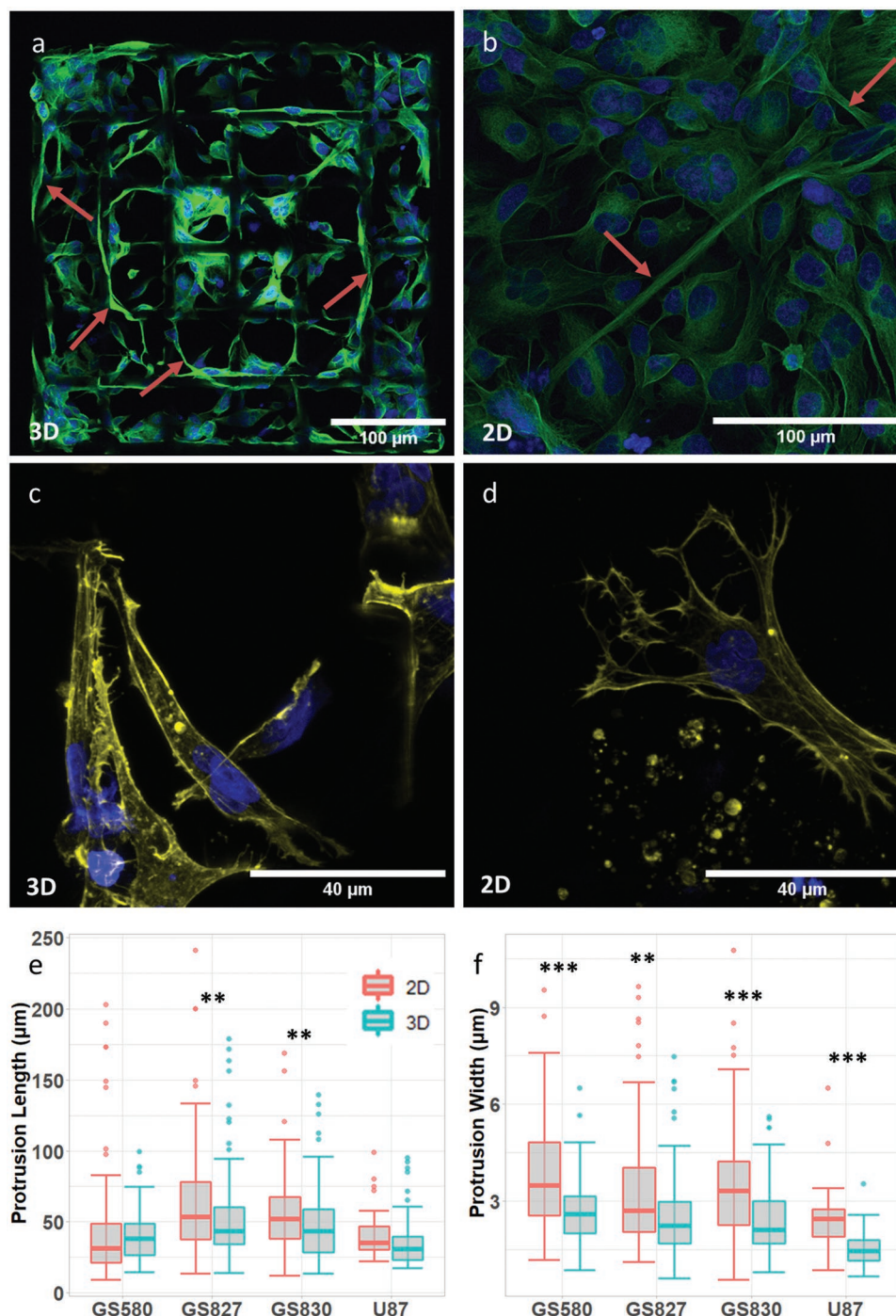
NANO · MICRO

small

www.small-journal.com

Figure 5. Characterization of microtube-like protrusions in patient derived glioma cells cultured on 2D pedestals and 3D scaffolds. a–d) Confocal images of patient-derived glioma cells on 2D pedestals and 3D scaffolds (Blue: nuclei; Green: tubulin; Yellow: Gap-43). Microtube-like protrusions were observed on GS-827 cells cultured on (a) the 3D scaffolds and (b) the 2D pedestals. Gap-43 staining was observed on cell membrane for GS-830 cells cultured on (c) the 3D scaffolds and (d) the 2D pedestals. e,f) Boxplots comparing microtube morphology. e) Protrusion length, and (f) protrusion width. Boxplots display the median, IQR with the whiskers drawn at 1.5IQR. Statistical significance is indicated by $p < 0.01$ (**) and $p < 0.001$(***). Sample size (n) for protrusion length in GS580, GS287, GS830, and U87 are 191, 257, 247, and 106, respectively. Sample size for protrusion width in GS580, GS287, GS830, and U87 are 184, 214, 336, and 68 respectively. Two independent experimental replicates (one replicate for U-87 experiments) were included.

be noted that the lengths of protrusions in 3D scaffolds were likely underestimated because the measurements were based on Z projections.

The width of protrusions showed differences between cells cultured on 2D pedestals versus 3D scaffolds for all cultures with significantly thinner protrusions observed for 3D scaffolds

(Figure 5f). The larger width of these protrusions in 2D pedestals may point to the flatter morphology of cells in 2D settings (similar to the observations on the cells and nuclei). Interestingly, the average measured protrusion width of 2.4 ± 1.1 µm in the 3D scaffolds was closer to the reported *in-vivo* value of 1.7 µm[51] and smaller than the 2D average value of 3.4 ± 1.7 µm. The morphology of the tube-like protrusions observed in 3D scaffolds therefore seems to better mimic what is described as microtubes in vivo[6,50] compared to those formed in 2D pedestals or even in other 3D culture models such as tumor organoids.[53] Moreover, these protrusions seem to be more abundant in our 3D scaffolds compared to the glioma spheroids[6] and glioma organoids.[53] It is also possible that these protrusions are simply easier to visualize in our model.

To evaluate the persistence of the cellular network and the possibility of tracking cells on the scaffolds, we employed live confocal imaging over a period of 16.5 h (**Figure 6**a,b). Migration of GS-830 cells in the $X–Y$ plane was tracked (Figure 6c) and compared between cells growing on 2D surfaces and 3D scaffolds (Figure 6d). On average, the speed of cells on 2D surfaces (4.2 ± 2.7 µm h⁻¹) was double the speed of cells on 3D scaffolds (2.1 ± 1.8 µm h⁻¹) (p-value < 0.0001). The speed of cells in the Z direction is not considered in these measurements, but manual tracking of 31 cells in 3D shows a Z speed of 1.1 ± 0.6 µm h⁻¹, which does not compensate for the difference between 2D and 3D. Even theoretically, with Z speeds similar to those observed in X and Y (1.5 µm h⁻¹), cells grown in 3D (2.6 µm h⁻¹) would still migrate slower than cells in 2D.

Cancer progression is affected by the cellular microenvironment.[2,13,54] For instance, glioma cells interact with the vascular niche and tend to move along the blood tracks and the white matter tracks.[28,55–57] Multiple studies have reported on the differences of cell migration between 2D and 3D environments.[58–60] GS-830 cells in our 3D model moved along the scaffold rods (Movie S4, Supporting Information) and occasionally established protrusions between the rods (Figure S8, Movie S5, Supporting Information). This cell migration on the scaffolds was reminiscent of cells on the brain tissue,[57] whereas
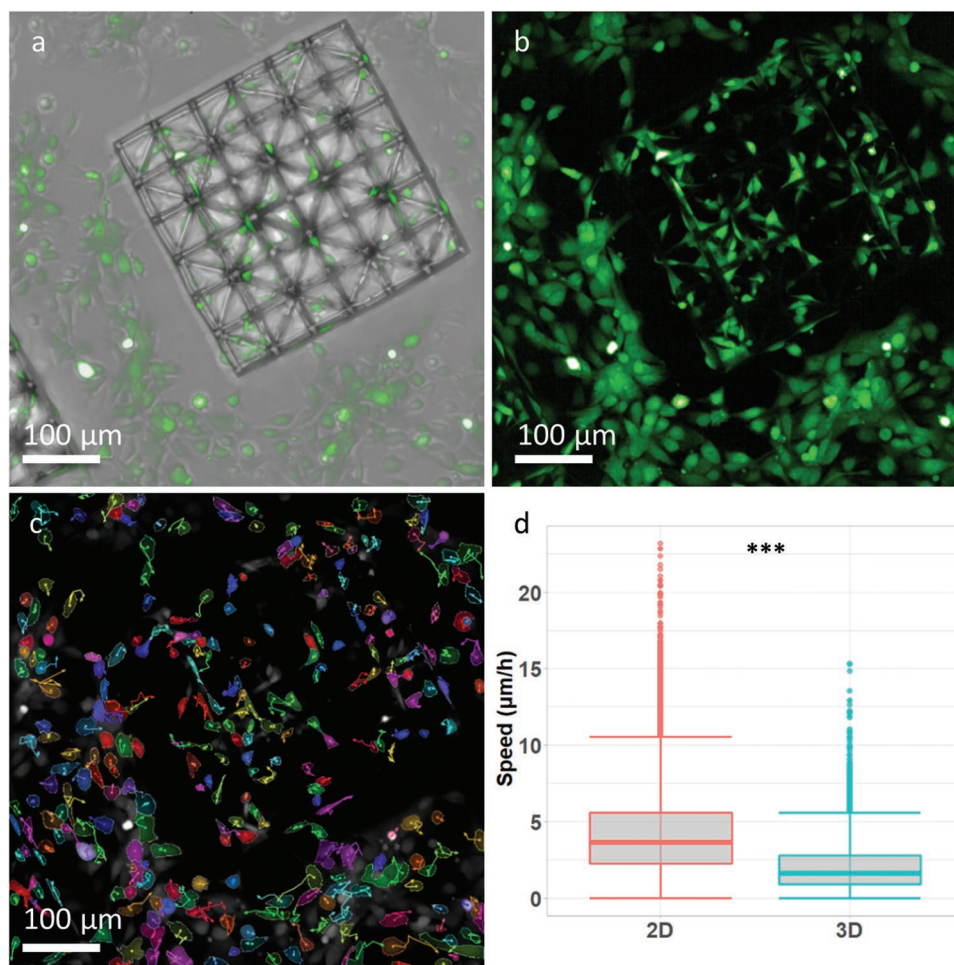

Figure 6. Tracking the movement of patient-derived glioma cells on 3D scaffolds and 2D surfaces. a,b) Representative frame of the live experiment showing GS-830 glioma cells on 3D scaffolds and on the surrounding 2D surface (Green: glioma cells stained with CellTracker Green). a) Brightfield and fluorescent maximum intensity projection image showing glioma cells on 3D scaffolds. (b) Fluorescent maximum intensity projection image of the cells. c) Movements of individual cells tracked on the 3D scaffolds and the surrounding 2D surface. d) Boxplot comparing $X–Y$ speed of cells cultured on 2D and 3D structures. Boxplots display the median, IQR with the whiskers drawn at 1.5IQR. Statistical significance is indicated by $p < 0.001$(***). Sample size (n) is 47 447.

**ADVANCED
SCIENCE NEWS**
www.advancedsciencenews.com

**NANO · MICRO
small**
www.small-journal.com

the movement of the cells on 2D surfaces appeared to be more random (Movie S6, Supporting Information) and this difference was consistent with previous reports.[59]

Strikingly however, individual cellular protrusions were more stable in 3D, where those in 2D had a shorter half-life (12.8 ± 3.9 vs 7.9 ± 4.6 hours, p-value = 0.006) (Figure S9, Supporting Information), suggesting a more stable network of cells grown on 3D scaffolds. Furthermore, compared to 2D surfaces, within the 3D scaffolds we observed slower cell migration and protrusions that last longer, therefore the presence of a more stable cellular network in the 3D scaffolds.

2.5. Differential Distribution of EGFR on 3D Scaffolds and 2D Pedestals

EGFR is one of the most commonly altered receptors in gliomas.[11,61,62] Therefore, we next assessed the potential of the model in capturing the subcellular localization of EGFR. In the presence of the EGFR ligand, epidermal growth factor (EGF), EGFR was present in spots that were distributed throughout the cells but concentrated close to the nuclei on both scaffolds and pedestals (**Figure 7**a; Figure S10, Supporting Information). These spots were also detectable on long cellular protrusions in cells cultured on the 3D scaffolds (Figure 7b) but were hardly detectable on long protrusions in cells cultured on the 2D pedestals (Figure S10, Supporting Information). Two independent EGFR antibodies (ab76153 Abcam and M3563 DAKO), stained on the same sample, showed a near identical staining pattern (Figure 7c,d). When EGF was absent from the culture media (for duration of three days), only a few EGFR spots remained and general plasma membrane staining was observed, in line with the ligand-induced internalization of the receptor (Figure 7e,f).

To evaluate our model's ability in drug screening, we then tested two known EGFR tyrosine kinase inhibitors (TKIs), Erlotinib, and Dacomitinib. In this experiment, GS-830 cells were seeded on the 2D pedestals and the 3D scaffolds under four conditions: i) with EGF in the culture media (+EGF, control experiment), ii) without EGF in the culture media (−EGF), iii) with Erlotinib added to the +EGF culture media for 2 h (+Erlotinib), and iv) with Dacomitinib added to the +EGF culture media for 2 h (+Dacomitinib) (**Figure 8**). Interestingly, even in the presence of Erlotinib or Dacomitinib, some (perinuclear) spots were present in cells. Although there were fewer internalized EGFR spots, they did not completely disappear (**Figure 9**a). The perinuclear EGFR spots remained even when the exposure time to Dacomitinib was increased from 2 to 24 h (Figure S11, Supporting Information). For all conditions except for −EGF, the Kolmogorov–Smirnov test showed that the distance of EGFR spots to the cell nuclei for 2D versus 3D cultures came from separate distributions (+EGF: p-value < 0.0001, −EGF: p-value < 0.0001, +Erlotinib: p-value < 0.0001, +Dacomitinib: p-value < 0.0001). The Kruskal–Wallis test showed that the difference of medians of this distance between 2D and 3D structures were statistically significant in all conditions except for +EGF condition (Figure 9b). Although EGFR spot localizations on 2D and 3D structures were similar, in most conditions, spots were larger and had lower signal intensity in 2D experiments
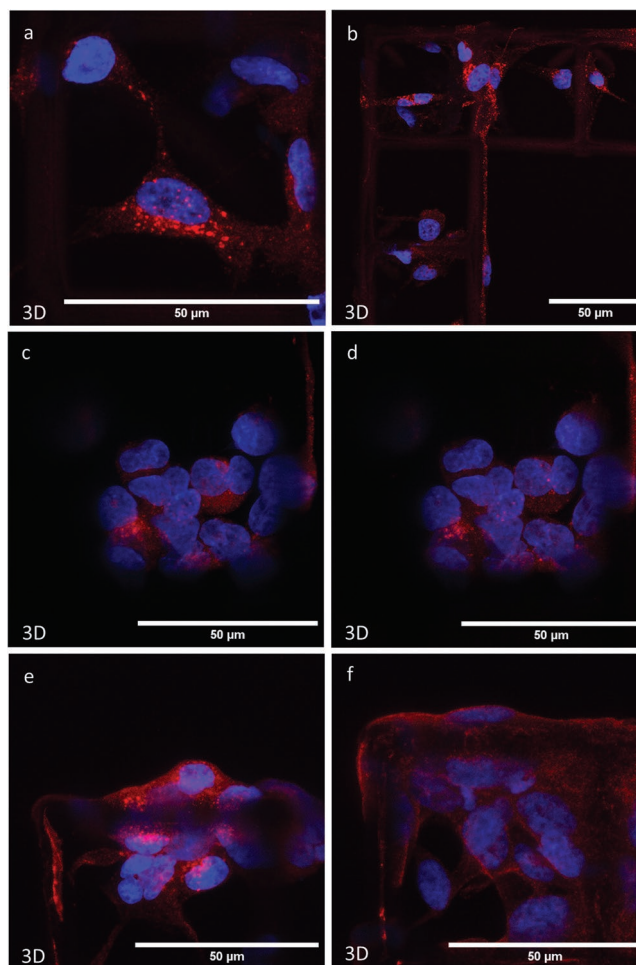

Figure 7. Characterization of EGFR expression on GS-830 cells cultured on 3D scaffolds. a) Zoomed in confocal image showing EGFR spots close to the nuclei on a 3D scaffold. b) EGFR spots observed in cellular protrusions. c,d) GS-830 cells stained using two different EGFR antibodies, which both give similar signals. c) Anti-EGFR Abcam ab76153, d) anti-EGFR DAKO M3563. e,f) Fewer EGFR spots are observed in the absence of EGF. (e) Cells cultured in the presence of EGF. (f) Cells cultured in the absence of EGF (Blue: nuclei; Red: EGFR).

(Figure 9c,d). Additionally, spot detection in 3D was superior due to higher signal-to-noise ratio, possibly because of the autofluorescence signal of the material in 2D. Interestingly, in the +EGF condition, a negative correlation ($\rho = −0.13$, p-value < 0.0001) was observed between the distances of EGFR spots to the nuclei and the brightness of the spots (Figure 9e). Generally, brighter spots were not detected far from the nuclei (Figure 9e). Same negative correlation was observed, but with lower correlation coefficient, in the presence of Erlotinib ($\rho = −0.10$, p-value < 0.0001) or Dacomitinib ($\rho = −0.05$, p-value = 0.01), but was not significant for the −EGF condition ($\rho = −0.04$, p-value = 0.25) (Figure S12, Supporting Information).

The EGFR spots observed in our experiments (+EGF conditions) are consistent with endocytosed EGFR proteins.[63–68] Endocytosed EGFR can either be recycled back to the membrane (either fast or slow recycling) or can be directed toward degradation.[69] Our data suggests that at least part of the
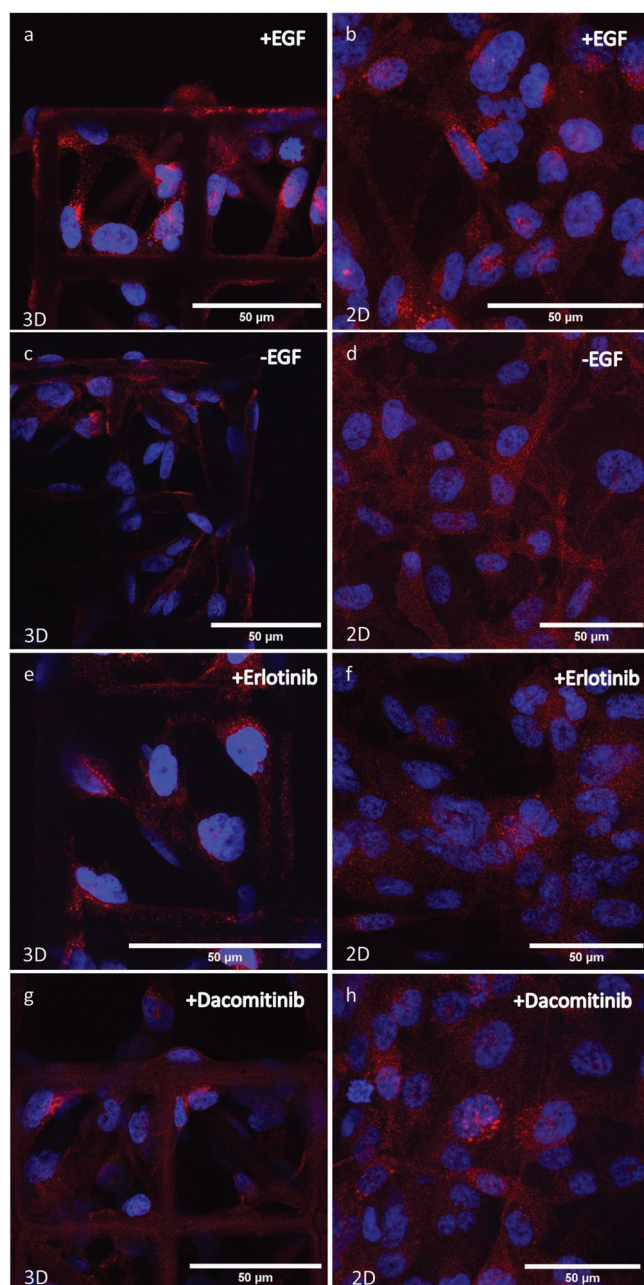
Figure 8. Representative confocal images of GS-830 cells with and without EGF/EGFR inhibitors. Exposure time to inhibitors was 2 h. a) Image of the cells on the 3D scaffold and in presence of EGF. b) Image of the cells on the 2D pedestal and in presence of EGF. c) Image of the cells on the 3D scaffold without EGF. d) Image of the cells on the 2D pedestal without EGF. e) Image of the cells on the 3D scaffold with EGF and Erlotinib. f) Image of the cells on the 2D pedestal with EGF and Erlotinib. g) Image of the cells on the 3D scaffold with EGF and Dacomitinib. h) Image of the cells on the 2D pedestal with EGF and Dacomitinib (Blue: nuclei; Red: EGFR).

EGFR is directed to the perinuclear endosomal sorting compartment[70] and this localization is not entirely inhibited by TKIs. Although the function of the subcellular localization is unknown, several reports have suggested the importance of EGFR localization near the nuclei in patient outcome and

tumor progression.[63,64,71,72] The 3D-engineered scaffolds offer a platform in which the EGFR localization can be tracked and analyzed in vitro, in 3D and with high resolution. The use of these scaffolds for live imaging of the EGFR spots and tracking their transfer to the nuclear area may add to our understanding of their functions and of the resistance to EGFR inhibition in patients.[10,73–76]

3. Conclusions

In conclusion, we designed and engineered 3D-microscaffolds, fabricated by the 2PP method, and showed that they can be used to successfully culture and analyze patient-derived glioma cells. The design of the biomimetic scaffolds is inspired by the geometry of microvessel architecture in the brain. These structures are reproducible and biocompatible, and the low-auto-fluorescence nature of the employed biomaterial enables an accurate detection of fluorescent markers. The scaffolds offer the opportunity to study patient-derived glioma cells with morphological features more similar to those observed in glioma tumor cells in vivo. A major advantage of our scaffold approach is that it enabled the study of (EGFR in) individual cells within a connected cellular network, whereas in conventional 2D cultures this is more error prone due to overlapping cells. These scaffolds could also be used to study nano- and microtube dynamics, cell networks, and cell migration strategies as they better represented the dimensionality of 3D tumor microenvironments, enable tracking of individual cells and provide more stable cell networks. Such features are much more difficult to study in conventional 2D "petri-dish" and 3D spheroid model systems. Therefore, the developed scaffolds offer new insights on glioma cell-to-cell and cell-to-environment interactions in three dimensions. In the future, our 3D-engineered culture model will be further improved by coculturing glioma cells with other nontumor cells, such as endothelial cells and immune cells, which are predicted to have roles in glioma prognosis.

4. Experimental Section

Scaffold Design and Fabrication: The 3D-engineered scaffolds and the 2D pedestals were fabricated with the 2PP method. The scaffolds and the pedestals were designed using a computer aided design (CAD) software, SolidWorks (Dassault Systèmes, France). A Standard Triangle Language file from the CAD software was then imported to the DeScribe software (Nanoscribe, Germany). The resulting General Writing Language file was imported to Nanowrite (printing software, Nanoscribe, Germany) directly from DeScribe.

For the fabrication, the Photonic Professional GT+ printer (Nanoscribe, Germany) was used in Dip-in Laser Lithography configuration with a 25× objective featuring 0.8 numerical aperture. IP-Visio (Nanoscribe, Germany), a methacrylate photosensitive polymer, was casted on indium-tin oxide (ITO)-coated glass substrates (dimensions of 25 mm × 25 mm × 0.7 mm, Nanoscribe, Germany).

Before printing, the ITO-coated substrates (resistance of 100 to 400 Ω) went through a few preparatory steps. First, the substrates were cleaned by acetone and ISO-Propanol (IPA). Then, the ITO-coated side was blow-dried with a nitrogen gun. Next, for further substrate activation, the ITO-coated side of the substrates was exposed to oxygen plasma for the duration of 10 min at 80 W power with 5 sccm oxygen flow rate and pressure of 0.12 bar. Then, the substrates were silanized
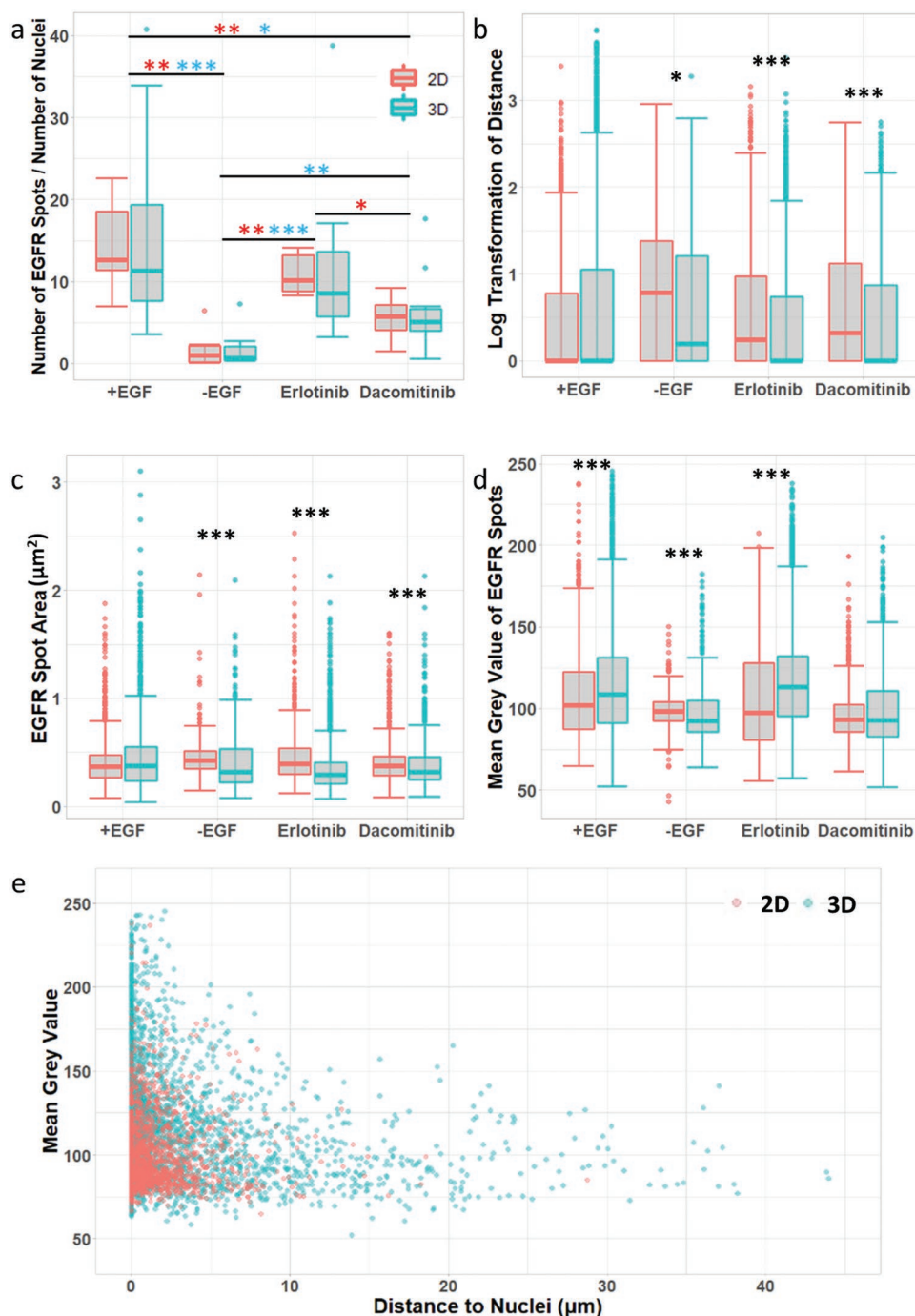
**ADVANCED
SCIENCE NEWS**

www.advancedsciencenews.com

NANO · MICRO

small

www.small-journal.com

Figure 9. Characterization of EGFR spot localization on GS-830 cells cultured on 2D pedestals and 3D scaffolds. a) Boxplots of number of EGFR spots per number of nuclei in each image. Red asterisks show significance between conditions in 2D pedestals and blue asterisks show significance between conditions on 3D scaffolds. b) Boxplots of distances of EGFR spots to the nuclei in 2D and 3D conditions. Value of 0 for the distance means that in the Z projection of images, the spot was situated in the nucleus region. c) Boxplots of areas of EGFR spots. d) Boxplots of mean gray values of EGFR spots. The value shows the average signal intensity of a selected region. e) Dot plot of EGFR spot mean gray value versus EGFR spot distance to the nucleus in +EGF condition. Boxplots display the median, IQR with the whiskers drawn at 1.5IQR. Statistical significance is indicated by $p < 0.05$ (*), $p < 0.01$ (**), and $p < 0.001$(***). Sample size (n) for (a) for +EGF, −EGF, +Erlotinib, +Dacomitinib are 22, 15, 19, and 16, respectively. Sample size for (b–d) for +EGF, −EGF, +Erlotinib, and +Dacomitinib are 6979, 811, 5324, and 2639, respectively. Sample size for (e) is 6979. Two independent experimental replicates were included.

to make the substrate surface hydrophobic and enable a chemical bond between the polymerized 2PP resin and the substrate itself. The silanization solution consisted of ethanol and 3-(trimethoxysilyl) propyl methacrylate (#440159, Sigma-Aldrich, USA). The dipping time and the

concentration of the solution were 1 h and 2% v/v 3-(trimethoxysilyl) propyl methacrylate in ethanol, respectively.[77] After silanization, the samples were rinsed first with acetone, then with water, and finally air-dried for ≈5 min. Immediately after drying, the resin was placed on the

ADVANCED
SCIENCE NEWS
www.advancedsciencenews.com

NANO · MICRO
small
www.small-journal.com

substrates and the samples were placed in the Nanoscribe printer for fabrication. Several printing and geometrical parameters were tested to obtain a suitable print quality (Figure S13, Supporting Information). The details of these parameters are presented in Section 2.1.

After fabrication, to remove the unpolymerized resin, samples were immersed in propylene glycol methyl ether acetate for 30 min. They were then immediately rinsed in IPA for 5 min. Later, samples were left in a fume hood to air-dry. To fit the samples in 6-well cell culture plates (used for culturing and immunofluorescence staining steps), the corners of the ITO-coated glass were scraped by creating diagonal lines with a diamond pen cutter. The corners were then broken off with tweezers. To fit the samples in 24-well cell culture plates (used for live cell confocal imaging), the ITO-coated glass was cut into 4 mm × 13 mm rectangles with an in-house femtosecond laser cutter.

The samples were visually inspected to be free from defects such as breakage, deformity, delamination, and geometrical flaws. Optical microscopy with 10× or 20× magnification was employed for quick inspections and the fabrication quality was checked more extensively by SEM.

Glioblastoma Cell Culture: Four patient-derived glioma cell cultures, GS-830, GS-580, GS-827, and GS-921, alongside U87 standard cell line were tested. GS-830 and GS-921 are isocitrate dehydrogenase (IDH)-wild-type glioblastoma cells, and GS-580 and GS-827 are IDH-mutant astrocytomas.[5,78] EGFR is expressed in both (IDH)-wild-type and (IDH)-mutant cell cultures used in the experiments, but EGFR amplification is lost in culture.[78] The use of patient tissue was approved by the Medical Ethical Review Committee Erasmus MC, code MEC-2013-090, and all patients signed informed consent forms according to the guidelines of the Institutional review board.

The cell culture steps were adopted from a published protocol.[5,78] Unless otherwise specified, 20 ng mL^{-1} basic fibroblast growth factor, 20 ng mL^{-1} EGF, and 5 μg mL^{-1} heparin was used in Dulbecco's modified Eagle medium/Nutrient Mixture F-12 (DMEM/F-12, 11320-033, Gibco, USA) as the cell culture media. Each sample set, containing three scaffolds and four pedestals fabricated on one ITO substrate, was placed in one well of a 6-well plate and washed with ethanol 70% followed by two washes with phosphate buffered saline (PBS). Structures were coated with Cultrex Basement Membrane Extract Reduced Growth Factor (3500-096-01, Trevigen, USA). This coating is cell line derived and consists of a mixture of extracellular matrix proteins such as laminin and collagen IV. For this experiment, 100 μL coating solution (1:100 Cultrex coating diluted in culture media) was used to cover the surface of each substrate. In the meantime, cells were kept in flasks until they reached 80% confluency. At that time, 1 mL of cell suspension (1 000 000 cells mL^{-1}) was seeded on each coated sample set. 2 mL cell culture medium was then added to each well. For experiments with Dacomitinib (S2727, Selleckchem, USA) and Erlotinib (S1023, Selleckchem, USA), 10 μM of the inhibitors was added to the culture medium 2 h before cell fixation. For -EGF conditions, cell culture media was used without the addition of EGF.

Scanning Electron Microscopy: For SEM imaging of cells seeded on the fabricated structures, the cells were fixed and dehydrated. Concerning cell fixation, cell culture medium was removed and samples were washed two times with PBS. Then, 2% paraformaldehyde was added for 30 min followed by 4% glutaraldehyde for 2 h. Scaffolds and cells within them were then washed two times with PBS and dehydrated sequentially in 50% ethanol (15′), 70% ethanol (20′), and ethanol (20′) and dried at room temperature.

SEM was employed to assess the fabrication quality of the structures and the cell–microstructure interaction. To avoid charge build-up, the samples were sputter-coated with a gold nanolayer. A Sputter Coater JEOL JFC-1300 (Tokyo, Japan) was used for this purpose. All samples were coated once horizontally and two times in opposing 45° tilted configurations in order to ensure a homogeneous metal coating also along sidewalls. In the horizontal configuration, the samples were sputter-coated using a 20 mA current for 20 s adding ≈13 nm thick gold layer. The duration was reduced to 10 s for each tilted configuration adding ≈6.5 nm thick gold layer.

For SEM imaging, secondary electron generated images were recorded using a JEOL JSM-6010LA scanning electron microscope (Tokyo, Japan). Concerning the recorded images, the accelerating voltage ranged from 10 to 20 kV and the spot size (diameter of the electron beam) ranged from 50 down to 30 nm.

Immunofluorescence Staining and Confocal Imaging Configuration: Primary antibodies were anti-Beta-Tubulin (ab6046, Abcam, UK, 1:200 dilution), anti-GAP-43 (8945, Cell Signaling Company, USA, 1:200 dilution), and anti-EGFR (M3563, DAKO, Germany, 1:500 dilution, or ab76153, Abcam, UK, 1:200 dilution). Secondary antibodies were Alexa Flour 488 anti-rabbit (A11008, Life Technologies, USA, 1:500 dilution) and Alexa Fluor 647 anti-mouse (A21240, Life Technologies, USA, 1:500 dilution). The anti-EGFR made by Abcam provided stronger signals and therefore was preferred. All antibodies were diluted in PBS with 1% W/V bovine serum albumin. Samples were incubated with primary or secondary antibodies each for 1 h at room temperature in humidity chambers. Scaffolds were mounted with Vectrashield fluorescent mounting with DAPI (Vector Laboratories, USA) for the visualization of nuclei. A coverglass was placed on top of the scaffolds. In order to prevent damaging the scaffolds during imaging, two spacers (Imaging Spacers, GBL654002, Grace Bio-Labs, USA) with the thickness of 120 μm were used (Figure S14, Supporting Information). An oil immersion upright microscope Stellaris 5 (Leica Microsystems, Germany) with 40× objective and numerical aperture 1.30 was used for confocal immunofluorescent imaging. To avoid cross-talk between channels, the imaging for individual markers was carried out sequentially.

Staining of FFPE tissue slices was performed for tumor cell marker IDH (DIA-H09, Dianova, USA, for IDH-mutant, low grade tissue slices) or Glial Fibrillary Acidic Protein (GFAP, M0761, DAKO, Germany, for IDH-wildtype, high grade tumors) and nuclear counterstaining with DAPI. Staining was performed on 4 μm FFPE sections as previously described.[79] Staining for tumor marker was performed by antigen retrieval with microwave treatment in AR6 buffer (AR600250ML, Akoya Biosciences, USA), blocking (ARD1001EA, Akoya Biosciences, USA), primary antibody incubation (1:20 for IDH and 1:50 for GFAP, diluted in blocking solution), secondary antibody incubation (ARH1001EA, Akoya Biosciences, USA), and subsequent incubation with tyramide signal amplification plus fluorophore (OP-001006, Akoya Biosciences, 1:100, diluted in amplification diluent FP1498, Akoya Biosciences), with washing steps in between. Finally, sections were counterstained with spectral DAPI (Spectral DAPI, FP1490, AKOYA Biosciences, USA) and mounted with mounting medium (P36970, Invitrogen, USA). Following staining, whole sections were scanned (10× magnification) and representative sections per patient (three low grade and three high grade patients) were imaged in higher magnification (20×; area: 690 × 516 μm; resolution: 2 pixels μm^{-1}, pixel size: 0.5 × 0.5 μm^2) with the use of Vectra 3.0 (Akoya Biosciences, Menlo Park, CA, USA) as previously described.[79] Images were manually thresholded for identification of tumor marker positive regions, and nuclei in these regions were identified using the Stardist plugin.[80] These images were then exported to be used for downstream image analysis.

Live Confocal Imaging: Prior to cell seeding, cells were stained with a fluorescent dye, CellTracker Green CMFDA Dye (C2925, Invitrogen, USA), diluted in DMEM/F-12 medium (5 μM) and were incubated for 30 min at 37 °C. Next, this mixture was replaced with normal medium and the cells were seeded on the scaffolds according to the stated cell culture protocol. Cells were left to grow and attach to the scaffolds in an upright configuration for ≈16 h. Then the samples were flipped upside down for imaging (Figure S15, Supporting Information). To keep samples in the inverted configuration, Grace Bio-Labs imaging spacers were used. Three scaffolds and the 2D surfaces were imaged every 1.5 h for a total of 16.5 h using Opera Phenix High-Content Screening System (Perkin Elmer, USA) with an inverted 20× objective and 0.4 numerical aperture.

Image Analysis: Concerning fluorescent images, the analysis was performed on maximum intensity Z projections of stacks of image slices. Images were analyzed using ImageJ software (National Institutes of Health, USA). Macrocodes were developed to extract and quantify the features of interest from each image (nucleus size, circularity, EGFR "spot" size, fluorescence intensity, and location). All codes are explained

in the Supporting Information. The Stardist plug-in was used for nuclei segmentation.[80] The cell area was defined as the combination of nuclei and tubulin areas. Circularity, used to quantify nuclei and cell circularity, is defined in ImageJ software as $4\pi(A\,P^{-2})$, where A is area and P is perimeter. To quantify the EGFR localization, a combination of Stardist for nuclei detection,[80] ComDet for EGFR spot detection,[81] and NearestNeighbour to find distances was used.[82] All tube-like protrusions were marked in ImageJ based on the tubulin staining and were quantified in terms of length and width. For this, fluorescent images (with 380 μm × 380 μm field of view) of the stained cells on 2D pedestals and 3D scaffolds were recorded and then analyzed. All experiments were independently replicated at different points in time using subsequent passage numbers to colonize the scaffolds. All conditions within one experiment (i.e., cultured ± EGF, +Erlotinib, +Dacomitinib) were simultaneously performed, processed, and imaged using identical imaging parameters.

Harmony high-content imaging and analysis software (Perkin Elmer, USA) was used to analyze the live experiment images. Position and speed of the cells on 2D and 3D structures were tracked and recorded based on the maximum intensity Z projections of stacks of image slices. Analysis is explained in more detail in the Supporting Information.

Statistical Analysis: The data were analyzed with R programming using RStudio. The Shapiro–Wilk test was used to verify normal distribution of data ($p < 0.05$). A one-way analysis of variance test for normal data and a Kruskal–Wallis test for non-normal data were used. The Kolmogorov–Smirnov test was used to compare the distribution of data sets. Spearman's rank-order correlation test was used to find correlation between variables with non-normal distributions. Statistical significance was set at $p < 0.05$ (*), $p < 0.01$ (**), and $p < 0.001$(***). Sample size (n) for each test is displayed in the related figure legends. Boxplots display the median, interquartile range (IQR) with the whiskers drawn at 1.5IQR.

Supporting Information

Supporting Information is available from the Wiley Online Library or from the author.

Conflict of Interest

The authors declare no conflict of interest.

Data Availability Statement

The data that support the findings of this study are available from the corresponding author upon reasonable request.

[1] Q. T. Ostrom, L. Bauchet, F. G. Davis, I. Deltour, J. L. Fisher, C. E. Langer, M. Pekmezci, J. A. Schwartzbaum, M. C. Turner, K. M. Walsh, M. R. Wrensch, J. S. Barnholtz-Sloan, *Neuro. Oncol.* **2014**, *16*, 896.

[2] S. Caragher, A. J. Chalmers, N. Gomez-Roman, *Cancers* **2019**, *11*, 44.

[3] M. L. Goodenberger, R. B. Jenkins, *Cancer Genet.* **2012**, *205*, 613.

[4] B. W. Stringer, B. W. Day, R. C. J. D'Souza, P. R. Jamieson, K. S. Ensbey, Z. C. Bruce, Y. C. Lim, K. Goasdoué, C. Offenhäuser, S. Akgül, S. Allan, T. Robertson, P. Lucas, G. Tollesson, S. Campbell, C. Winter, H. Do, A. Dobrovic, P. L. Inglis, R. L. Jeffree, T. G. Johns, A. W. Boyd, *Sci. Rep.* **2019**, *9*, 4902.

[5] C. Verheul, I. Ntafoulis, T. V. Kers, Y. Hoogstrate, P. G. Mastroberardino, S. Barnhoorn, C. Payán-Gómez, R. T. C. Yen, E. A. Struys, S. L. W. Koolen, C. M. F. Dirven, S. Leenstra, P. J. French, M. L. M. Lamfers, *Neurooncol Adv.* **2021**, *3*, 103.

[6] S. Weil, M. Osswald, G. Solecki, J. Grosch, E. Jung, D. Lemke, M. Ratliff, D. Hänggi, W. Wick, F. Winkler, *Neuro Oncol.* **2017**, *19*, 1316.

[7] A. Pandita, K. D. Aldape, G. Zadeh, A. Guha, C. D. James, *Genes Chromosomes Cancer.* **2004**, *39*, 29.

[8] M. Osswald, G. Solecki, W. Wick, F. Winkler, *Neuro Oncol.* **2016**, *18*, 479.

[9] M. Schneider, F. A. Giordano, T. Kuner, W. Wick, U. Herrlinger, F. Winkler, *Nat. Rev. Cancer* **2022**, *22*, 481.

[10] E. Eskilsson, G. V. Røsland, G. Solecki, Q. Wang, P. N. Harter, G. Graziani, R. G. W. Verhaak, F. Winkler, R. Bjerkvig, H. Miletic, *Neuro Oncol.* **2018**, *20*, 743.

[11] W. Szopa, T. A. Burley, G. Kramer-Marek, W. Kaspera, *Biomed. Res. Int.* **2017**, *2017*, 8013575.

[12] J. M. Heffernan, D. J. Verstreet, L. D. Le, B. L. Vernon, R. W. Sirianni, *Ann. Biomed. Eng.* **2015**, *43*, 1965.

[13] K. A. Jansen, D. M. Donato, H. E. Balcioglu, T. Schmidt, E. H. J. Danen, G. H. Koenderink, *Biochim. Biophys. Acta, Mol. Cell Res.* **2015**, *1853*, 3043.

[14] R. Edmondson, J. J. Broglie, A. F. Adcock, L. Yang, *Assay Drug Dev. Technol.* **2014**, *12*, 207.

[15] N. Gomez-Roman, K. Stevenson, L. Gilmour, G. Hamilton, A. J. Chalmers, *Neuro Oncol.* **2017**, *19*, iii26.

[16] C. Jensen, Y. Teng, *Front. Mol. Biosci.* **2020**, *7*, 33.

[17] L. Ma, B. Zhang, C. Zhou, Y. Li, B. Li, M. Yu, Y. Luo, L. Gao, D. Zhang, Q. Xue, Q. Qiu, B. Lin, J. Zou, H. Yang, *Colloids Surf., B* **2018**, *172*, 665.

[18] E. D. Lemma, B. Spagnolo, M. De Vittorio, F. Pisanello, *Trends Biotechnol.* **2019**, *37*, 358.

[19] D. Fan, U. Staufer, A. Accardo, *Bioengineering* **2019**, *6*, 133.

[20] W. S. Harley, C. C. Li, J. Toombs, C. D. O'Connell, H. K. Taylor, D. E. Heath, D. J. Collins, *Int. J. Bioprint.* **2021**, *23*, 00147.

[21] A. Accardo, M. C. Blatché, R. Courson, I. Loubinoux, C. Vieu, L. Malaquin, *Mater. Today* **2018**, *21*, 315.

[22] A. Accardo, R. Courson, R. Riesco, V. Raimbault, L. Malaquin, *Addit. Manuf.* **2018**, *22*, 440.

[23] Q. Akolawala, M. Rovituso, H. H. Versteeg, A. M. R. Rondon, A. Accardo, *ACS Appl. Mater. Interfaces* **2022**, *14*, 20778.

[24] A. K. Nguyen, R. J. Narayan, *Mater. Today* **2017**, *20*, 314.

[25] A. Accardo, M. Blatché, R. Courson, I. Loubinoux, C. Vieu, L. Malaquin, *Biomed. Phys. Eng. Express* **2018**, *4*, 027009.

[26] C. Liao, A. Wuethrich, M. Trau, *Appl. Mater. Today* **2020**, *19*, 100635.

[27] Nanoscribe, "Resins for Printing, IP-Visio," https://support.nanoscribe.com/hc/en-gb/articles/360011709499-IP-Visio#Ch:IPVisio_general (accessed: February 2021).

[28] A. Farin, S. O. Suzuki, M. Weiker, J. E. Goldman, J. N. Bruce, P. Canoll, *Glia* **2006**, *53*, 799.

[29] Y. Yang, S. Motte, L. J. Kaufman, *Biomaterials* **2010**, *31*, 5678.

[30] Nanoscribe, "NanoGuide CAD Model Creation," https://support.nanoscribe.com/hc/en-gb/articles/360000810253-CAD-Model-Creation (accessed: April 2021).

[31] J. Song, C. Michas, C. S. Chen, A. E. White, M. W. Grinstaff, *Adv. Healthcare Mater.* **2020**, *9*, 2192.

[32] A. J. Engler, S. Sen, H. L. Sweeney, D. E. Discher, *Cell* **2006**, *126*, 677.

[33] A. I. Ciuciu, P. J. Cywiński, *RSC Adv.* **2014**, *4*, 45504.

[34] A. Sharaf, B. Roos, R. Timmerman, G.-J. Kremers, J. Bajramovic, A. Accardo, *Front. Bioeng. Biotechnol.* **2022**, *10*, 926642.

[35] M. Tromayer, A. Dobos, P. Gruber, A. Ajami, R. Dedic, A. Ovsianikov, R. Liska, *Polym. Chem.* **2018**, *9*, 3108.

[36] A. Ovsianikov, S. Mühleder, J. Torgersen, Z. Li, X. H. Qin, S. Van Vlierberghe, P. Dubruel, W. Holnthoner, H. Redl, R. Liska, J. Stampfl, *Langmuir* **2014**, *30*, 3787.

[37] O. Tolde, D. Rösel, R. Janoštiak, P. Veselý, J. Brábek, *Folia Biol.* **2012**, *58*, 177.

[38] M. Babi, R. Riesco, L. Boyer, A. Fatona, A. Accardo, L. Malaquin, J. Moran-Mirabal, *ACS Appl. Bio Mater.* **2021**, *4*, 8443.

[39] R. Nafe, K. Franz, W. Schlote, B. Schneider, *Clin. Cancer Res.* **2005**, *11*, 2141.

[40] L. Liu, Q. Luo, J. Sun, G. Song, *Exp. Cell Res.* **2016**, *348*, 56.

[41] T. P. Driscoll, B. D. Cosgrove, S. J. Heo, Z. E. Shurden, R. L. Mauck, *Biophys. J.* **2015**, *108*, 2783.

[42] M. Webster, K. L. Wikin, O. Cohen-Fix, *J. Cell Sci.* **2009**, *122*, 1477.

[43] S. Cho, J. Irianto, D. E. Discher, *J. Cell Biol.* **2017**, *216*, 305.

[44] D. H. Kim, D. Wirtz, *Biomaterials* **2015**, *48*, 161.

[45] D. B. Lovett, N. Shekhar, J. A. Nickerson, K. J. Roux, T. Lele, *Cell. Mol. Bioeng.* **2013**, *6*, 230.

[46] D. M. Graham, K. Burridge, *Curr. Opin. Cell Biol.* **2016**, *40*, 98.

[47] K. Miranda, D. A. Pace, R. Cintron, J. C. F. Rodrigues, J. Fang, A. Smith, P. Rohloff, E. Coelho, F. De Haas, D. Souza, I. Coppens, L. D. Sibley, S. N. J. Moreno, *Science* **2013**, *341*, 1240104.

[48] P. Jevtić, L. J. Edens, L. D. Vuković, D. L. Levy, *Curr. Opin. Cell Biol.* **2014**, *28*, 16.

[49] D. Boruah, P. Deb, *ISRN Oncol.* **2013**, *2013*, 760653.

[50] M. Osswald, E. Jung, F. Sahm, G. Solecki, V. Venkataramani, J. Blaes, S. Weil, H. Horstmann, B. Wiestler, M. Syed, L. Huang, M. Ratliff, K. Karimian Jazi, F. T. Kurz, T. Schmenger, D. Lemke, M. Gömmel, M. Pauli, Y. Liao, P. Häring, S. Pusch, V. Herl, C. Steinhäuser, D. Krunic, M. Jarahian, H. Miletic, A. S. Berghoff, O. Griesbeck, G. Kalamakis, O. Garaschuk, et al., *Nature* **2015**, *528*, 93.

[51] M. Osswald, E. Jung, W. Wick, F. Winkler, *Cancer Rep.* **2019**, *2*, 1181.

[52] L. I. Benowitz, A. Routtenberg, *Trends Neurosci.* **1997**, *20*, 84.

[53] G. Pinto, I. Saenz-De-Santa-Maria, P. Chastagner, E. Perthame, C. Delmas, C. Toulas, E. Moyal-Jonathan-Cohen, C. Brou, C. Zurzolo, *Biochem. J.* **2021**, *478*, 21.

[54] A. Vollmann-Zwerenz, V. Leidgens, G. Feliciello, C. A. Klein, P. Hau, *Int. J. Mol. Sci.* **2020**, *21*, 1932.

[55] C. Calabrese, H. Poppleton, M. Kocak, T. L. Hogg, C. Fuller, B. Hamner, E. Y. Oh, M. W. Gaber, D. Finklestein, M. Allen, A. Frank, I. T. Bayazitov, S. S. Zakharenko, A. Gajjar, A. Davidoff, R. J. Gilbertson, *Cancer Cell* **2007**, *11*, 69.

[56] Y. Yi, I. Y. Hsieh, X. Huang, J. Li, W. Zhao, *Front. Pharmacol.* **2016**, *7*, 477.

[57] C. J. Liu, G. A. Shamsan, T. Akkin, D. J. Odde, *Biophys. J.* **2019**, *117*, 1179.

[58] P. Friedl, E. Sahai, S. Weiss, K. M. Yamada, *Nat. Rev. Mol. Cell Biol.* **2012**, *13*, 743.

[59] P.-H. Wu, A. Giri, S. X. Sun, D. Wirtz, *Proc. Natl. Acad. Sci. USA* **2014**, *111*, 3949.

[60] S. I. Fraley, Y. Feng, R. Krishnamurthy, D. H. Kim, A. Celedon, G. D. Longmore, D. Wirtz, *Nat. Cell Biol.* **2010**, *12*, 598.

[61] S. Sigismund, D. Avanzato, L. Lanzetti, *Mol. Oncol.* **2018**, *12*, 3.

[62] P. C. Pan, R. S. Magge, *Int. J. Mol. Sci.* **2020**, *21*, 8471.

[63] W. Xia, Y. Wei, Y. Du, J. Liu, B. Chang, N. L. Yu, L. F. Huo, M. C. Hung, *Mol. Carcinog.* **2009**, *48*, 610.

[64] I. Hadžisejdi, E. Mustać, N. Jonjić, M. Petković, B. Grahovac, *Mod. Pathol.* **2010**, *23*, 392.

[65] S. Scharaw, M. Iskar, A. Ori, G. Boncompain, V. Laketa, I. Poser, E. Lundberg, F. Perez, M. Beck, P. Bork, R. Pepperkok, *J. Cell Biol.* **2016**, *215*, 543.

[66] I. Pinilla-Macua, A. Grassart, U. Duvvuri, S. C. Watkins, A. Sorkin, *eLife* **2017**, *6*, 31993.

[67] B. M. Chung, S. M. Raja, R. J. Clubb, C. Tu, M. George, V. Band, H. Band, *BMC Cell Biol.* **2009**, *10*, 84.

[68] T. Tanaka, Y. Zhou, T. Ozawa, R. Okizono, A. Banba, T. Yamamura, E. Oga, A. Muraguchi, H. Sakurai, *J. Biol. Chem.* **2018**, *293*, 2288.

[69] J. Bakker, M. Spits, J. Neefjes, I. Berlin, *J. Cell Sci.* **2017**, *130*, 4087.

[70] A. Baldys, J. R. Raymond, *Biochemistry* **2009**, *48*, 9321.

[71] T. Brand, M. Iida, N. Luthar, M. Starr, E. Huppert, D. Wheeler, *Radiother. Oncol.* **2013**, *108*, 370.

[72] A. Tomas, C. E. Futter, E. R. Eden, *Trends Cell Biol.* **2014**, *24*, 26.

[73] S. Mazzoleni, L. S. Politi, M. Pala, M. Cominelli, A. Franzin, L. S. Sergi, A. Falini, M. De Palma, A. Bulfone, P. L. Poliani, R. Galli, *Cancer Res.* **2010**, *70*, 7500.

[74] Y. Gao, W. R. Vallentgoed, P. J. French, *Cancers* **2018**, *10*, 489.

[75] A. H. Thorne, C. Zanca, F. Furnari, *Neuro Oncol.* **2016**, *18*, 914.

[76] A. A. Brandes, E. Franceschi, A. Tosoni, M. E. Hegi, R. Stupp, *Clin. Cancer Res.* **2008**, *14*, 957.

[77] X. Liu, H. Gu, M. Wang, X. Du, B. Gao, A. Elbaz, L. Sun, J. Liao, P. Xiao, Z. Gu, *Adv. Mater.* **2018**, *30*, 1800103.

[78] R. K. Balvers, A. Kleijn, J. J. Kloezeman, P. J. French, A. Kremer, M. J. Van Den Bent, C. M. F. Dirven, S. Leenstra, M. L. M. Lamfers, *Neuro Oncol.* **2013**, *15*, 1684.

[79] C. Phanthunane, R. Wijers, M. de Herdt, T. P. M. Langeveld, S. Koljenovic, S. Dasgupta, S. Sleijfer, R. J. Baatenburg de Jong, J. Hardillo, H. E. Balcioglu, R. Debets, *Oncoimmunology* **2021**, *10*, 1882743.

[80] U. Schmidt, M. Weigert, C. Broaddus, G. Myers, presented at the Int. Conf. on Medical Image Computing and Computer-Assisted Intervention (MICCAI), Granada, Spain, September 2018.

[81] E. Katrukha, ComDet plugin for ImageJ, v0.5.3 2020, https://github.com/ekatrukha/ComDet (accessed: February 2022).

[82] ErasmusOIC, Simple nearest neighbour plugIn for ImageJ, https://github.com/ErasmusOIC/NearestNeighbour (accessed: December 2021).